Nanoscale Advances

ROYAL SOCIETY OF CHEMISTRY

PAPER

View Article Online
View Journal | View Issue

Cite this: *Nanoscale Adv.*, 2024, **6**, 5348

Synergistic atom co-sharing and S-scheme heterojunction: constructing Cu/CuO/Cu_2O with ultrathin graphene-like carbon derived from basil seeds for enhanced photo-oxidation of benzyl alcohols to aldehydes

Zahra Kohansal Nalkyashree,[a] Nadiya Koukabi,*[a] Kheibar Dashtian *[b] and Farzad Seidi [c]

This study is centered on the oxidative transformation of alcohols into their respective aldehyde compounds, employing an S-scheme heterostructure featuring CuO/Cu_2O on graphene-like carbon (GLC) derived from a basil seed hydrogel. Experimental characterization and theoretical calculations highlight that the implementation of S-scheme heterostructures achieves not only enhanced charge-separation efficiency, facilitated by the interfacial built-in electric field, Cu co-sharing at the CuO/Cu_2O interface, and electron carrier activity of the GLC support, but also maintains a strong driving force for photocatalytic organic conversion. The resulting nanocomposites play a crucial role in transferring and reducing the recombination of photoexcited charge carriers, preserving the oxidizability of CuO holes and the reducibility of Cu_2O electrons. Through meticulous adjustment of precursor amounts, the CuO–Cu_2O/GLC heterojunction exhibited the highest photocurrent at 6.83 mA cm^{-2}, demonstrating optimal performance in the photocatalytic selective oxidation of benzyl alcohol with an average conversion rate of 95.0%. Furthermore, the stability of CuO–Cu_2O/GLC was thoroughly investigated, revealing sustained high conversion even after five repeated experiments, underscoring its potential for practical applications. The study also proposes a plausible mechanism for the transformation of benzyl alcohol into benzaldehyde through capture experiments of active species. Importantly, this research introduces a straightforward *in situ* hydrothermal growth protocol for efficiently constructing metal oxide heterostructures wrapped in an rGO support. It provides valuable insights into designing new synthetic strategies for preparing efficient photocatalysts and hints at the development of novel, efficient, and practical photocatalytic systems.

Received 3rd April 2024
Accepted 20th July 2024

DOI: 10.1039/d4na00283k

rsc.li/nanoscale-advances

1. Introduction

The oxidation of alcohols to aldehydes holds significant importance in organic reactions.[1,2] Particularly, benzaldehyde stands out as a valuable industrial compound, serving as a key precursor in the production of various chemicals vital to the pharmaceutical and food industries.[3,4] Achieving controlled oxidation to benzaldehyde from benzyl alcohol remains a considerable challenge.[5] In industrial processes, the conventional method for alcohol oxidation to aldehydes typically involves high reaction temperatures and the use of high-valence metal salts as oxidants. This approach, characterized by high energy consumption, inevitably leads to the generation of environmental pollutants containing metal ions with high valence.[6–8] In contrast, multiphase visible light-driven photocatalysis has emerged as a promising green synthesis method, offering milder conditions.[9,10] This method harnesses naturally derived light energy to induce a catalytic effect, stimulating surrounding oxygen and water molecules into highly oxidizing free anions without generating harmful organic substances.[11] Typically, on pure semiconductors, the recombination of photogenerated electron and hole pairs is effortless, resulting in low photocatalytic efficiency which significantly hampers practical activity.[12] Hence, developing a rational and distinctive composite heterostructure design for the photocatalyst is deemed crucial for enhancing surface catalytic reactions. In recent years, engineering heterojunction interfaces has emerged as a highly favorable strategy in the design of

[a]Department of Chemistry, Semnan University, P.O. Box 35131-19111, Semnan, Iran. E-mail: n.koukabi@semnan.ac.ir

[b]Department of Chemistry, Iran University of Science and Technology, Tehran, 16846-13114, Iran. E-mail: kdasht68@gmail.com

[c]Jiangsu Co-Innovation Center of Efficient Processing and Utilization of Forest Resources and International Innovation Center for Forest Chemicals and Materials, Nanjing Forestry University, Nanjing 210037, China

photocatalysts.[13] This innovative approach aims to prevent electron–hole recombination, amplify charge migration and utilization, and enhance light harvesting, particularly in narrow band gap semiconductors.[14] Among various heterojunctions, such as Z-scheme, S-scheme, and type II, the development of S-scheme nanoheterojunctions through scientific methods is widely recognized as the most effective strategy for boosting the catalytic performance of photocatalysts.[14,15] Therefore, constructing S-scheme heterojunctions can promote charge transfer, improve photocatalytic ability, and enhance photocatalytic stability.[16] However, achieving tight contact interfaces among semiconductors to promote charge transfer remains a challenge.[17] Thus, finding a material that can act as an electron mediator and strengthen interfacial contact with semiconductors could greatly enhance photocatalytic activity and photogenerated carrier migration efficiency.[18] Therefore, investigating the use of metallic nanoparticles as electronic mediators for semiconductors to construct S-scheme heterojunctions that are more conducive to charge transfer is worthwhile. Meanwhile, the S-scheme interface charge transport channel includes an internal electric field (IEF), which can modulate the photogenerated carriers at the heterojunction and improve charge migration efficiency.[16,19–21] These mechanisms facilitate the efficient utilization of low-energy charge carriers generated by light, ensuring spatial separation and preservation of high-energy electron–hole pairs.[22,23] Moreover, in S-scheme heterojunctions where components share common atoms at the surface and co-share electrons, additional migration channels for photogenerated carriers are provided *in situ*.[24] This aspect promotes the migration and separation of photogenerated carriers, playing a crucial role in enhancing photoredox activity and photocatalytic efficiency.[25,26] In this context, heterojunctions based on multi-redox metal oxides,[13] chalcogenides,[27] and similar materials have emerged as favorable candidates. Among these materials, multi-redox metal oxides, especially those with the capability of atom co-sharing, stand out due to their higher stability and ease of synthesis.[28] However, challenges do arise in controlling their morphology, dispersibility, and mass transfer activity.[29] To address these challenges, the focus has shifted towards hierarchical self-supporting structures as a promising alternative in the design of metal oxide-based S-scheme nano-heterojunction photocatalysts.[30] These structures offer several advantages, including an enhanced specific surface area, increased availability of active sites, and improved mass transfer for catalytic reactions. The incorporation of hierarchical self-supporting structures addresses the challenges associated with morphology control, dispersibility, and mass transfer activity, making them a highly appealing choice for the development of efficient catalysts.[31]

In this context, hierarchical porous carbon, particularly graphene, is extensively employed as a support material for anchoring and stabilizing mixed metal oxide nano-heterojunctions. Graphene possesses exceptional properties, including a large specific surface area, high conductivity, and abundant surface defects, making it an ideal support material.[32] With a remarkable charge mobility of approximately 200 000 $cm^2\ V^{-1}\ s^{-1}$, graphene, with its exceptional surface area, exhibits characteristics such as chemical inertness, biocompatibility, thermal stability, and electron mediating capabilities. These qualities render graphene an excellent supporting matrix for bonding functional components.[33] Despite these advantages, the manufacturing processes for such materials in the presence of metal oxides often lack sufficient control over their textural characteristics, posing a challenge in achieving high graphitization and rich porosity in graphene.[34] Consequently, there is a pressing need for simple, secure, affordable, and environmentally friendly synthesis methods for these compounds. One promising approach involves utilizing biomass as a carbon source, leading to the generation of a hierarchical porous graphene-like carbon (GLC) network that can serve as a framework for metal oxide loading.[35] Recently, various types of biomasses such as peanut shells, peanut seed coats, and basil seeds have been used for generating GLC.[36–40] Among these, basil seeds (*Ocimum basilicum* L.), known for their mucilage content, are an inexpensive and readily available green precursor suitable for GLC production through the pyrolysis method.[13,41] The carboxylic acid and hydroxyl groups present in basil seeds are essential for metal ion insertion. This enhances catalyst dispersity, prevents aggregation, and mitigates charge recombination due to the carrier capabilities of graphene. Additionally, the hierarchical porous carbon network facilitates charge transfer between various nanograins and improves electron transmission by acting as a charge carrier.[42,43]

Herein, we have developed an S-scheme heterostructure that incorporates CuO/Cu_2O on graphene-like carbon (GLC), derived from a hydrogel based on basil seed biomass. The focus of this work is on demonstrating the effectiveness of S-scheme heterostructures in achieving improved charge-separation efficiency. This is facilitated by several factors, including the interfacial built-in electric field, Cu co-sharing at the CuO/Cu_2O interface, and the electron carrier activity of the GLC support. Importantly, these structures maintain a robust driving force for the photocatalytic reaction. The resulting nanocomposites play a critical role in transferring and reducing the recombination of photoexcited charge carriers. Through meticulous adjustment of precursor amounts, the Cu–CuO–Cu_2O/GLC composite was applied for the photocatalytic selective oxidation of benzyl alcohol. This study also proposes a plausible mechanism for the transformation of benzyl alcohol (BA) into benzaldehyde (BAD), supported by capture experiments of active species. Significantly, our research introduces a straightforward *in situ* hydrothermal growth protocol for efficiently constructing metal oxide heterostructures wrapped in a GLC support. This method provides valuable insights into designing new synthetic strategies for preparing efficient photocatalysts and hints at the development of novel, efficient, and practical photocatalytic systems.

2. Experimental

2.1. Materials

Copper chloride dihydrate ($CuCl_2 \cdot 2H_2O$, 98%), 4-nitrobenzyl alcohol ($C_7H_7NO_3$, 99%), 4-chlorobenzyl alcohol (C_7H_7ClO, 99%), 4-methoxybenzyl alcohol ($C_8H_{10}O_2$, 98%), 4-methylbenzyl alcohol ($C_8H_{10}O$, 99%), 4-hydroxybenzyl alcohol ($C_7H_8O_2$, 99%),

2-hydroxybenzyl alcohol ($C_7H_8O_2$, 98%), 4-fluorobenzyl alcohol (C_7H_7FO, 98%), sodium hydroxide (NaOH, 50%), *tert*-butyl hydroperoxide (TBHP, 70%), disodium ethylene diamine tetra-acetic acid (EDTA 99%), isopropyl alcohol (IPA) at 99.9%, ascorbic acid (vitamin C, 98%), and acetonitrile (CH_3CN, 99.95%) were procured from Merck Company (Darmstadt, Germany), and basil seeds were sourced from the Semnan market.

2.2. Instrumentation

The UV thin-layer chromatography lamp, manufactured by Tabatab company, features two lamps with wavelengths of 254 nm and 365 nm. Aluminum/silica gel 60 F_{34} thin-layer chromatography sheets were used. The catalysts were investigated using FT-IR (Fourier transform infrared, Shimadzu 8400S FT-IR spectrometer), and spectra of all samples were obtained using KBr disks. Thermogravimetric analysis (TGA) was conducted in a Linseis PT1000 from 30 to 800 °C under an N_2 atmosphere at a heating rate of 10 °C min^{-1}. X-ray diffraction (XRD) patterns were acquired on a Philips instrument with a Cu Kα radiation source. Scanning electron microscopy (SEM) images were collected using a TESCAN MIRA3 electron microscope. Raman spectra were determined using a Raman spectrograph (LabRAM HR Evolution, Horiba, France). Transmission electron microscopy (TEM) images were obtained on a TEM Philips EM 208S, and the microstructure of the samples was observed by HR-TEM (JEM-2100 UHR, JEOL, Japan). For X-ray photoelectron spectroscopy (XPS), an AXIS UltraDLD spectrometer (Kratos, UK) with an Al Kα X-ray source was employed for data analysis. Nitrogen adsorption–desorption isotherms were obtained using a Belsorp mini II instrument from Japan. The UV-vis diffuse reflectance spectra (DRS) of the powders were assessed on a Sinco S4100 spectrophotometer using $BaSO_4$ as a reference. Blue LED lamps with an electric power of 3 watts and a vacuum tube furnace were also utilized in the experimental setup.

2.3. Preparation of the S-scheme Cu–CuO–Cu_2O/GLC heterostructure

To ensure the purity of the purchased basil seeds and prevent any contamination, they were immersed in ethanol. After a 10 minute soaking period, the seeds were filtered using Whatman filter paper and subsequently placed in an oven at 50 °C overnight. The S-scheme Cu–CuO–Cu_2O/GLC heterostructure was synthesized through a multi-step process. Initially, Cu ions were chelated with a 3D hydrogel network, leading to their immobilization with saturated Cu ions. The hydrogel was then calcined to yield the Cu–CuO–Cu_2O/GLC heterostructure. The detailed construction steps are illustrated in Fig. 1. For the preparation of the heterostructure, 0.3 g of basil seeds were soaked in 30 mL of deionized water (DI water) for 5 min to swell the outer layer and form a basil seed mucilage layer. The swelled basil seeds were collected and immersed in a 7.5 mL NaOH solution (0.4 M) for 30 min, followed by three rinses with DI water to eliminate any residual NaOH. The resulting activated hydrogel was saturated and mixed with 0.027 g (0.15 mmol) of $CuCl_2 \cdot 2H_2O$ powder under vigorous magnetic stirring for 60 min. This allowed the copper ions to infiltrate the swollen basil seed layers, resulting in blue basil seeds. After three additional rinses with DI water, the blue basil seeds were calcined at 550 °C for 1 hour in a tube furnace with continuous aeration at 400 mL min^{-1} N_2. The resulting Cu–CuO–Cu_2O/GLC heterostructure catalyst was then collected and stored under dry conditions at room temperature. This innovative technique represents a simple, environmentally friendly, and cost-effective strategy that utilizes water as the sole reaction medium.

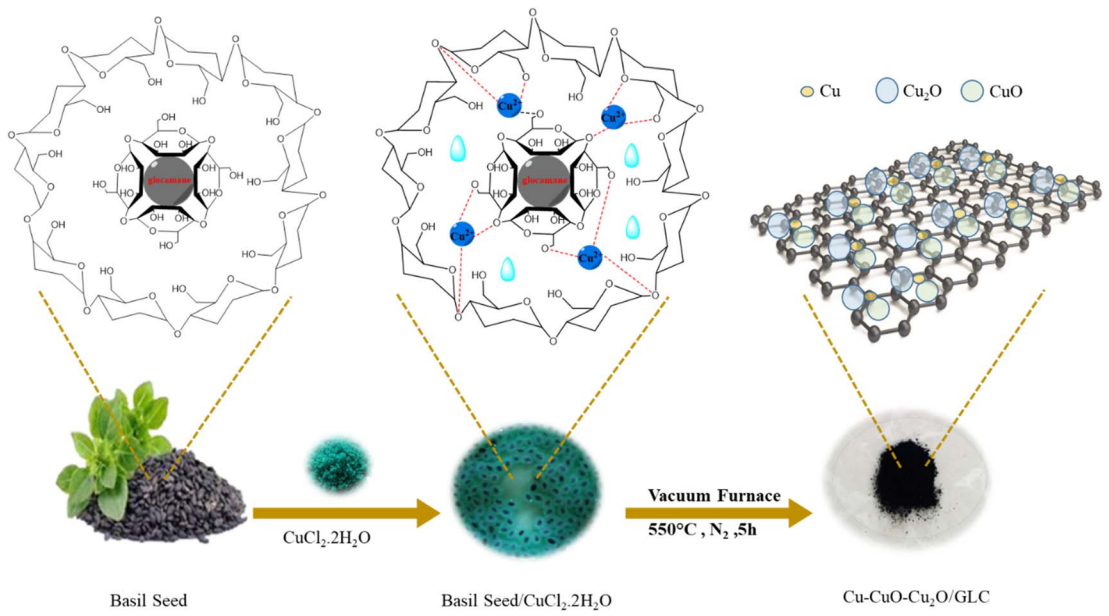

Fig. 1 Schematic diagram of Cu–CuO–Cu_2O/GLC S-scheme heterostructure photocatalyst synthesis.

2.4. General procedure for photocatalytic reaction

In the process of photocatalytic reaction within a Pyrex tube, 10 mg of the photocatalyst was introduced into a solution containing benzyl alcohol (0.5 mmol), TBHP (0.5 mmol) as the oxidant, and 1 mL of acetonitrile—an economical and less toxic solvent, all at room temperature. The reaction was initially conducted in the dark for 1 hour to establish equilibrium. The desorption and adsorption processes were facilitated by magnetic stirring. Subsequently, irradiation with a 4 × 3 W blue LED lamp (λ > 400 nm) was initiated at room temperature, and the reaction progress was monitored using thin-layer chromatography (TLC).

3. Results and discussion

3.1. Characterization of the photocatalyst

XRD analysis was utilized to characterize the crystalline structure of both basil seeds and the Cu–CuO–Cu_2O/GLC heterostructure catalyst (Fig. 2a). The XRD pattern of mountain basil seeds reveals an amorphous structure with very low crystallinity, corresponding to crystalline regions at 2θ = 15–30°.[44] In the XRD pattern of Cu–CuO–Cu_2O/GLC, peaks appeared at 2θ of 36.19°, 38.78°, 48.65°, 53.54°, 58.35°, and 61.34°, attributed to the crystal planes of (−111), (111), (−202), (020), (202), and (−113) of CuO nanoparticles, aligning with the JCPDS card (no. 00-003-0884).[45] Additionally, peaks at 2θ of 29.64°, 36.57°, 42.48°, and 61.64° related to the crystal planes of (110), (111), (200), and (220) confirm the presence of Cu_2O nanoparticles, consistent with the JCPDS card (no. 01-074-1230).[46] Peaks at 2θ = 43.47° and 50.37° correspond to the crystal planes of (110) and (111) of Cu nanoparticles, in agreement with the JCPDS card (no. 00-001-1241).[47] The presence of a distinct region at 24.5°–25.1° in the XRD analysis, precisely indexed to the (002) crystal planes, indicates the successful formation of GLC.[13]

FT-IR analysis was employed to examine the presence of functional groups in the prepared materials, confirming the successful fabrication and stepwise development of the catalyst, as illustrated in Fig. 2b. In the FT-IR spectrum of basil seeds, various characteristic bands were observed, including those at 1090 cm^{-1} (attributed to the C–O stretching mode), 1160 cm^{-1} (related to the C–O–C stretching mode, indicating the stretching vibrations of the polysaccharide glycosidic linkage), and 1240 cm^{-1} (representing C–H stretching vibrational modes).[48] Distinct bands at 1460 cm^{-1} and 1650 cm^{-1} signify uronic acid residues in the basil seed (C–OO asymmetric and symmetric band stretching vibrations). Furthermore, there are two peaks at 1542 cm^{-1} and 1745 cm^{-1}, corresponding to the stretching vibrations of the C=O symmetric and asymmetric atoms.[49] Additional features include peaks at 2855 cm^{-1} (C–H absorption), 2929 cm^{-1} (CH_2 bending vibrations), and 3010 cm^{-1} (C–H stretching vibration), as well as a broad band in the range of 3150–3550 cm^{-1}, signifying hydroxyl alcohol groups.[50] The presence of bands at 3330 and 3371 cm^{-1} is attributed to the tensile vibrations of OH (hydroxyl) on the surface of CuO–Cu_2O nanoparticles.[51]

Thermogravimetric analysis (TGA) and differential thermogravimetric analysis (DTG) were conducted to assess the thermal stability of the materials. In the TGA diagram of basil seeds (Fig. 2d), the degradation occurs in four stages. The weight loss within the range of 35–199 °C is attributed to moisture loss. The primary degradation stage, where the polymer structure disintegrates between 250 and 300 °C, is linked to the degradation of polysaccharides such as zeilan, glucan, and glucaminic acid. Subsequent degradation at 400–500 °C is associated with the breakdown of cellulose and lignin. The final stage involves degradation at 500–620 °C. Analyzing the TGA diagram of the Cu–CuO–Cu_2O/GLC catalyst (Fig. 2e), it is observed that in the temperature range of 50–350 °C, less than

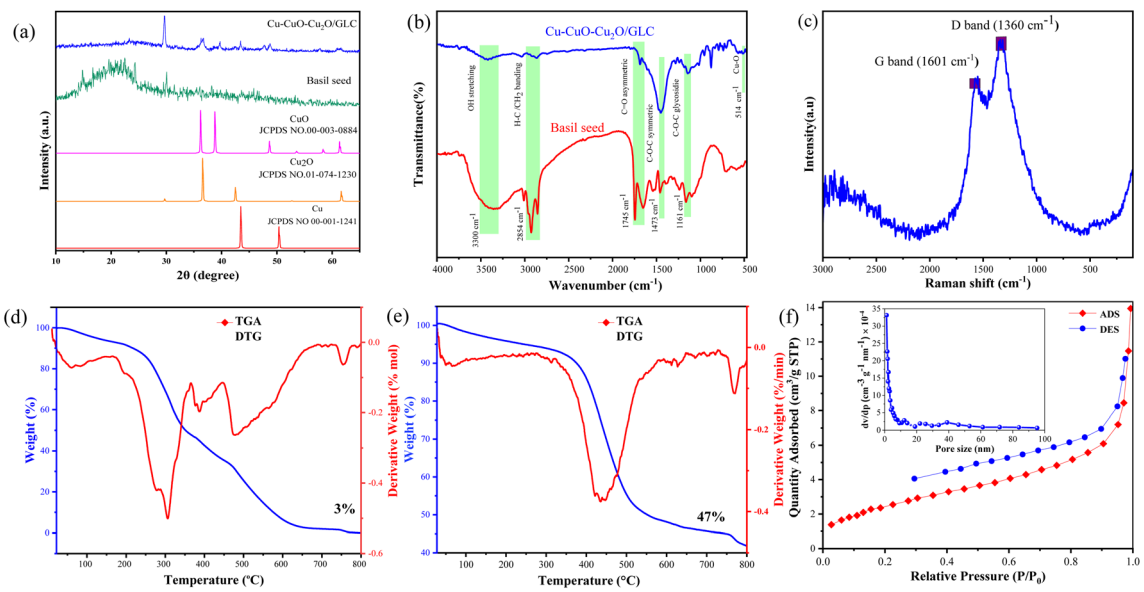

Fig. 2 XRD patterns (a), FT-IR spectra (b), Raman spectra (c), TGA and DTG curves (d and e), and nitrogen adsorption/desorption along with pore size distribution (f) of the pristine basil seed and S-scheme Cu–CuO–Cu_2O/GLC stereostructure.

4.8% of the sample weight is reduced due to the evaporation of coordinated water molecules. Gradual weight loss in the range of 350–500 °C indicates the combustion of carbon in the catalyst. After the formation of Cu–CuO–Cu_2O and the decomposition of the copper–carbon matrix, a stable profile emerges after 500 °C, signifying the formation of copper oxide. At a temperature of 800 °C, 45% of the catalyst remains, highlighting its robust stability compared to pristine basil seeds.

Raman spectroscopy was utilized to assess the degree of irregularity in the carbon structure. In the obtained spectrum, bands related to D (1362 cm^{-1}) and G (1621 cm^{-1}) of carbon compounds, especially graphene, were observed (Fig. 2e).[52]

For a comprehensive assessment of the surface area, porosity, and absorption–desorption characteristics, the specific surface area, diameter, volume, and size distribution of the catalyst pores were scrutinized using Brunauer–Emmett–Teller (BET) and Barrett–Joyner–Halenda (BJH) analyses. The evaluations were conducted at 77 K, employing nitrogen adsorption, and the corresponding graphs are illustrated in Fig. 2f. In the BET analysis chart, the sample exhibits a type III isotherm in accordance with the IUPAC classification. A noticeable increase in the volume of adsorbed nitrogen under the relative pressure p/p_0, particularly within the range of 0.001 to 0.7 in the isotherm, indicates the presence of numerous micropores. Furthermore, the isotherm displays hysteresis, signifying the existence of mesopores in the material. Specifically, the H3 hysteresis in this isotherm indicates the presence of open-ended mesopores (sheets) within the hydrogel, with a pore size of 8.35 nm (the BJH analysis results are shown in the inset in Fig. 2f).

FESEM and TEM were employed to scrutinize the morphology of the Cu–CuO–Cu_2O/GLC heterostructure. In the FE-SEM images of the basil seed, the fabricated substrate exhibits an irregular and heterogeneous structure with uneven pores and a rough surface (Fig. 3a). In the FE-SEM images of the desired composition, the Cu_2O and CuO nanoparticles display a smooth and rough spherical shape on the basil seed surface (Fig. 3c–e). TEM images further reveal the formation and dispersion of Cu, Cu_2O and CuO nanoparticles within the ultrathin sheet of the GLC matrix (Fig. 3f and g). These results

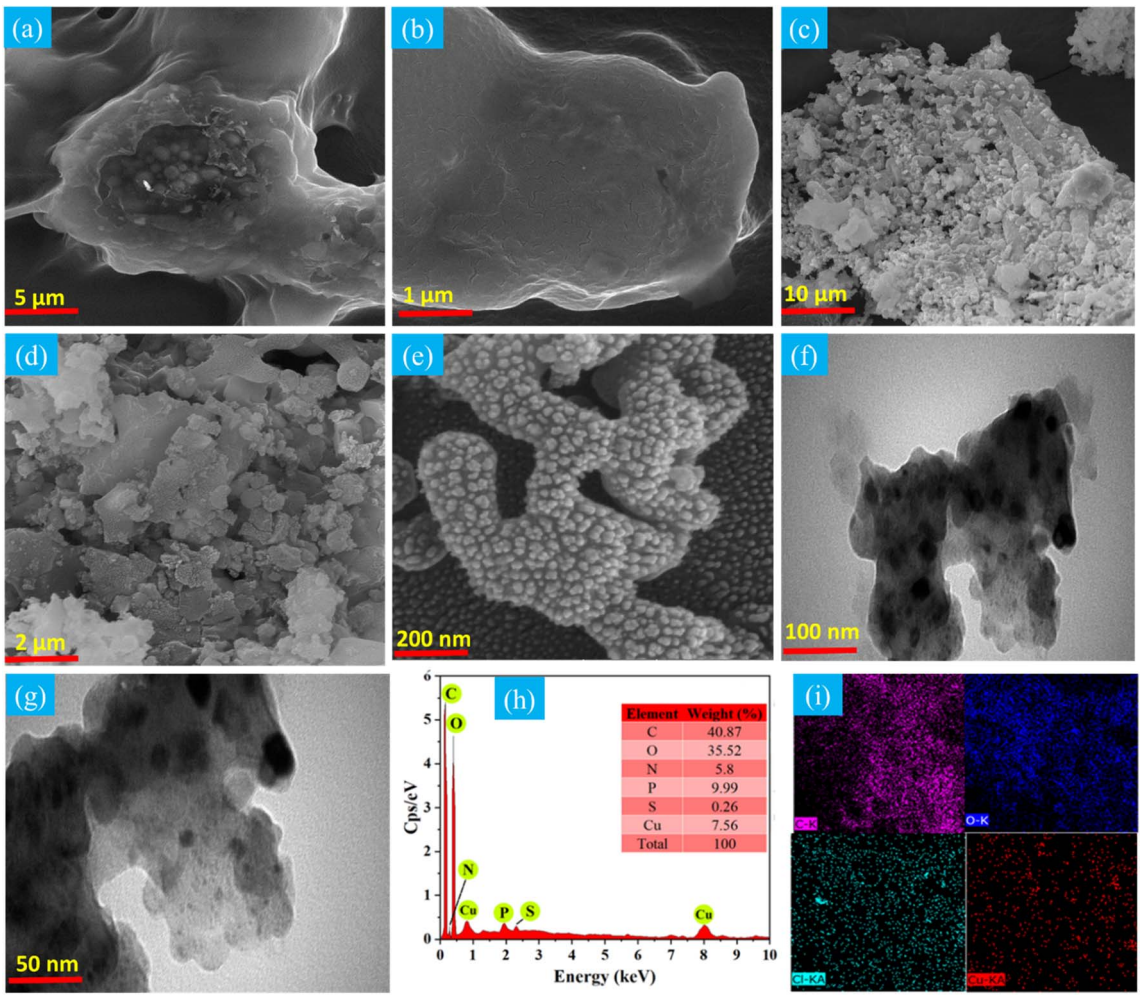

Fig. 3 FESEM images of basil seeds (a and b), FESEM images of the Cu–CuO–Cu_2O/GLC heterostructure (c–e), TEM images of the Cu–CuO–Cu_2O/GLC heterostructure (f and g), EDS spectrum (h), and EDS element mapping images of C, O, Cl, and Cu for the Cu–CuO–Cu_2O/GLC heterostructure (i).

substantiate that the prepared Cu-based catalyst is composed of crystals. For advanced chemical analysis, elemental mapping and EDS analysis were conducted to assess the atomic distribution, surface elemental content, and chemical composition of the synthesized catalysts. Fig. 3c and f showcase the EDS spectrum and elemental mapping images of the Cu–CuO–Cu_2O/GLC heterostructure, respectively, demonstrating the presence and homogeneous distribution of O, C, and Cu as the expected components. Trace amounts of S, N, and P were also detected, likely associated with the development and composition of the basil seed (Fig. 3f).

X-ray photoelectron spectroscopy (XPS) was employed to analyze the elemental composition and oxidation states of the Cu–CuO–Cu_2O/GLC heterostructure sample (Fig. 4). The XPS survey confirms the presence of Cu, O, and C elements (Fig. 4a). In the C 1s spectrum, the peaks in the region of 284, 285, 287, and 289 eV are attributed to C–C, C–OH, O–C=O, and C=O, respectively (Fig. 4b).[53] In the O 1s spectrum, the peaks observed in the region of 530, 531, 533, and 536 eV signify the bonding of Cu_2O, CuO, C=O, and O–H (Fig. 4c).[53,54] In the Cu 2p spectrum, the peaks with the binding energies of 933 and 934 eV are attributed to Cu $2p_{3/2}$, and the peaks in the region of 953 and 954 eV are attributed to Cu $2p_{1/2}$ in Cu_2O and CuO, respectively (Fig. 4d). The peaks located at 568.2, 568.5, and 569.5 eV were assigned to Cu^0, Cu^{2+}, and Cu^+, respectively. The satellite peak was observed at 942 and 962 eV (Fig. 4d).[55]

The band gap of Cu, Cu_2O, and CuO in combination with GLC, as well as in Cu–CuO–Cu_2O/GLC, was investigated using UV-vis diffuse reflectance spectroscopy. As depicted in Fig. 5a, all samples exhibited a significantly enhanced response to visible light. The bandgaps (E_g) of Cu, CuO, and Cu_2O nanoparticles in combination with GLC were estimated using Tauc plots, specifically by analyzing the curve of converted $(\alpha h\nu)^{1/n}$ *versus* $h\nu$ from their UV-vis DRS. The determined E_g values for CuO and Cu_2O were found to be 2.1 eV and 1.75 eV, respectively. The Cu nanoparticles exhibited metallic properties, measured by the *x*-axis intercept of extrapolated lines from the linear regimes of the curves (Fig. 2b). Additionally, both CuO/GLC and Cu_2O/GLC exhibited a negative slope in Mott–Schottky plots (data not shown), indicating their n-type nature. The flat band potentials (E_{fb}) of CuO/GLC and Cu_2O/GLC were determined to be −0.32 eV and −0.19 eV, respectively (*vs.* the normal hydrogen electrode, NHE, at pH 7), by measuring the *x*-axis intercepts of extrapolated lines from the linear regimes of the curves. In the Mott–Schottky plots of Cu–CuO–Cu_2O/GLC, the band bending at the semiconductor/electrolyte interface pushes electrons away from the interface while attracting holes (Fig. 5c). This illustrates how the E_{fb} of Cu–CuO–Cu_2O/GLC becomes slightly negative under light irradiation compared to that in the dark. Due to the low recombination of electron/hole pairs at the Cu–CuO–Cu_2O/GLC surface, the shift of E_{fb} is significant.

Based on the aforementioned findings, we successfully prepared a high-quality heterojunction involving Cu–CuO–Cu_2O/GLC in an S-scheme configuration. In order to understand the impact of this heterojunction on charge separation in the photocatalysts, a series of photoelectrochemical

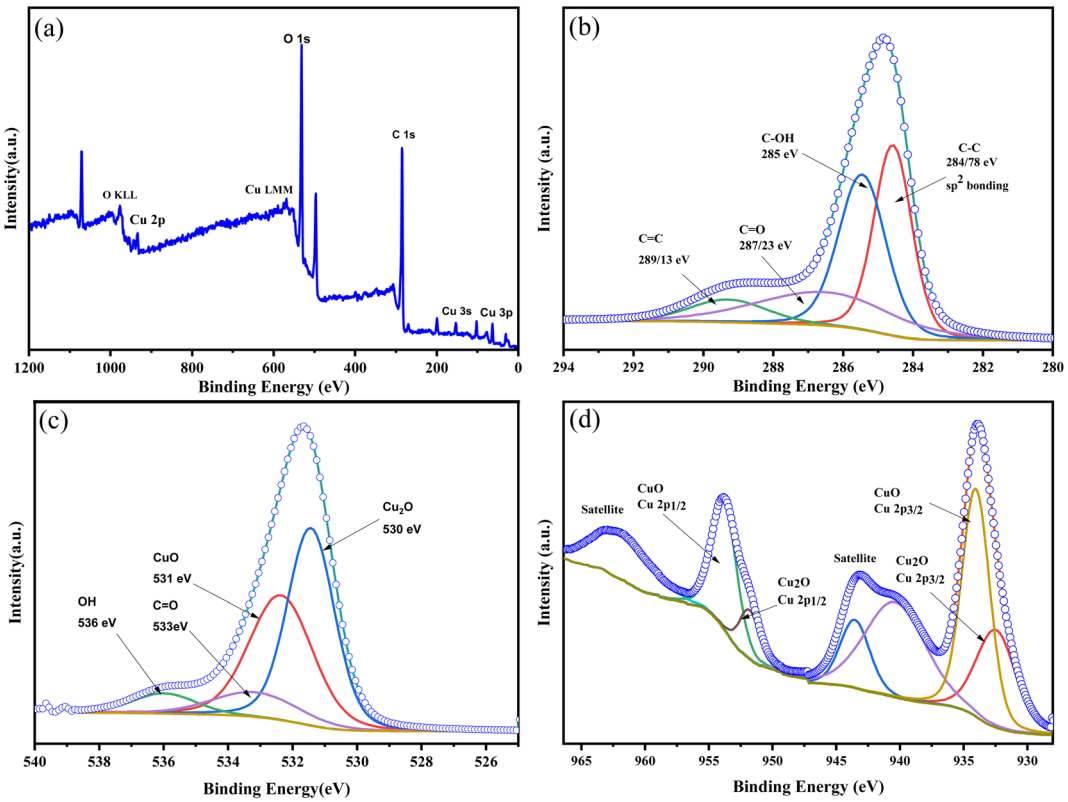

Fig. 4 XPS spectra of the Cu–CuO–Cu_2O/GLC S-scheme heterostructure: survey (a), C 1s (b), O 1s (c), and Cu 2p (d).

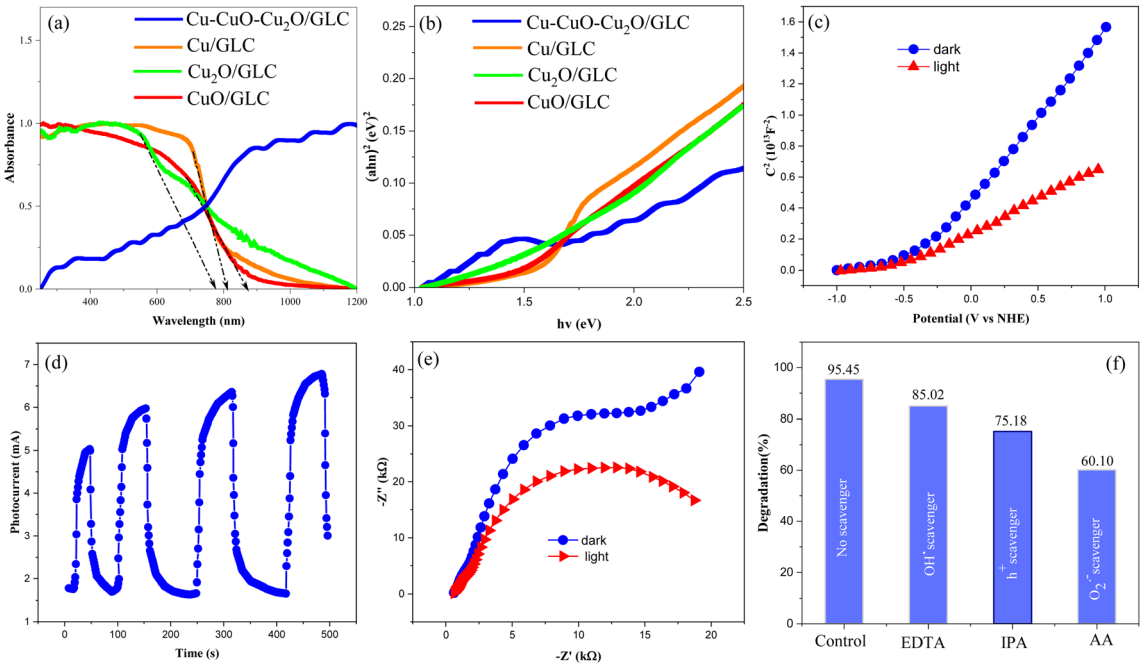

Fig. 5 DRS spectra (a), Tauc plot (b), Mott–Schottky plot (c), transient photocurrent (d) and EIS (e) of the as-prepared Cu–CuO–Cu_2O/GLC and scavenging experiments (f).

measurements were carried out to elucidate the charge transfer kinetics of the samples. In Fig. 5d, the photocurrent response of Cu–CuO–Cu_2O/GLC heterojunctions under blue-light irradiation is presented. Clearly, these heterojunctions exhibited a significantly intense photocurrent density, indicating the superior efficiency of charge carrier separation in the Cu–CuO–Cu_2O heterojunction. Moreover, the separation of photogenerated electrons (e^-) and holes (h^+) at the photocatalyst/electrolyte interface is evident in spikes observed in the current curve. These findings are further supported by electrochemical impedance spectroscopy (EIS) data, as illustrated in Fig. 5e. The Cu–CuO–Cu_2O/GLC heterojunction displayed a small semicircle, suggesting the lowest charge transfer resistance (R_{ct}). It is noteworthy that the R_{ct} of Cu–CuO–Cu_2O/GLC decreased under light irradiation, providing additional confirmation that the formation of a Cu atom co-sharing interface between CuO and Cu_2O reduces the S-scheme interfacial charge transfer resistance, along with enhancing the charge carrier mobility of graphene sheets. This reduction is advantageous for the effective separation and migration of photogenerated carriers.

3.2. Swelling ratio measurement

The swelling ratio (R_s) serves as a measurable parameter that quantifies the increase in mass or volume of a hydrogel. It can be determined using the formula $R_s = ((W_s - W_d)/W_d) \times 100$, where W_s represents the weight or volume of the swollen hydrogel, and W_d represents the weight or volume of the dry (unswollen) hydrogel. In the provided data, the hydrogel swelling ratio was found to be 1270 for the swollen BSH hydrogel and 775 for the swollen BSH hydrogel in the presence

Table 1 Optimization of reaction conditions for the alcohol oxidation reaction

Entry	Catalyst mass (g)	Light source	Solvent	Oxidant (mmol)	Yield (%)	Time (min)
1	—	Blue LED	Acetonitrile	*tert*-Butyl hydroperoxide	10	120
2	0.0075	Blue LED	Acetonitrile	*tert*-Butyl hydroperoxide	70	120
3	0.015	Blue LED	Acetonitrile	*tert*-Butyl hydroperoxide	90	140
4	0.01	Blue LED	Acetonitrile	*tert*-Butyl hydroperoxide	97	60
5	0.03	Blue LED	Acetonitrile	*tert*-Butyl hydroperoxide	95	90
6	0.01	Blue LED	Ethyl acetate	*tert*-Butyl hydroperoxide	70	120
7	0.01	Blue LED	Ethanol	*tert*-Butyl hydroperoxide	50	60
8	0.01	Blue LED	Solvent free	*tert*-Butyl hydroperoxide	50	120
9	**0.01**	**Visible light**	**Acetonitrile**	***tert*-Butyl hydroperoxide**	**95**	**20**
10	0.01	Green LED	Acetonitrile	*tert*-Butyl hydroperoxide	90	40
11	0.01	Sunlight	Acetonitrile	*tert*-Butyl hydroperoxide	80	90
12	0.01	Red LED	Acetonitrile	*tert*-Butyl hydroperoxide	90	90
13	0.01	Room light	Acetonitrile	*tert*-Butyl hydroperoxide	70	120

of copper(II) chloride. This suggests that the presence of copper(II) chloride significantly influences the swelling behavior of the hydrogel, leading to a reduction in the extent of swelling compared to the hydrogel without the copper compound.

3.3. Photocatalytic activity

Scavenging tests were initially conducted to identify the main active species responsible for the photocatalytic oxidation of alcohol to aldehyde using the Cu–CuO–Cu_2O/GLC heterostructure (Fig. 5f). Isopropyl alcohol (IPA), ethylenediaminetetraacetic acid (EDTA), and ascorbic acid (AA) were employed as scavengers for $O_2^{\bullet-}$, h^+, and $OH^\bullet$ respectively. The inclusion of AA and IPA resulted in a significant decrease in the rate of photocatalytic oxidation from alcohol to aldehyde, whereas EDTA had only a marginal impact on the efficiency of photo-oxidation. The results suggest that $O_2^{\bullet-}$ and h^+ are the main active species in photo-oxidation, while $OH^\bullet$ does not contribute to the photo-oxidation process. In cases where $O_2^{\bullet-}$

Table 2 Yield and reaction time of various benzyl alcohol derivatives[a]

No.	Reactant	Product	LED color	Yield (%)	Time (min)
1	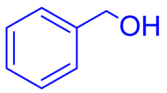	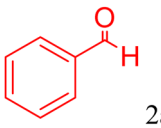 2a	Visible light Sunlight Blue light	95 80 97	20 90 60
2	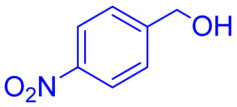	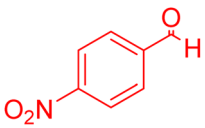 2b	Visible light Sunlight Blue light	50 50 60	10 60 60
3	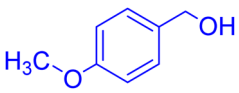	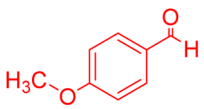 2c	Visible light Sunlight Blue light	70 60 60	10 10 10
4	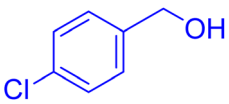	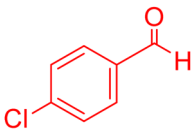 2d	Visible light Sunlight Blue light	60 60 60	60 60 60
5	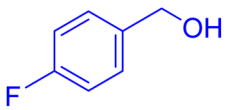	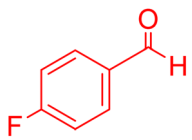 2e	Visible light Sunlight Blue light	70 50 50	60 10 15
6	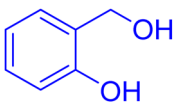	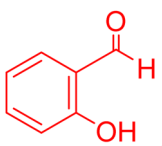 2f	Visible light Sunlight Blue light	75 65 55	60 60 60
7	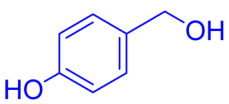	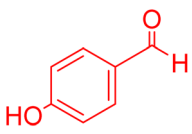 2g	Visible light Sunlight Blue light	70 60 50	60 60 60
8	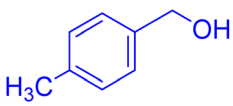	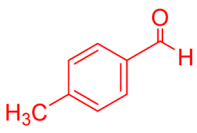 2h	Visible light Sunlight Blue light	60 70 80	60 20 60

[a] Reaction conditions: benzyl alcohol (0.5 mmol), acetonitrile (1 mL), *tert*-butyl hydroperoxide (1.5 mmol), and catalyst (1 mg).

and h^+ were scavenged, there was an increase in the conversion rate of aldehyde to alcohol efficiency.

Following the confirmation of product synthesis, repeated tests were conducted with varying catalyst quantities to identify the optimal amount that would yield the highest efficiency. The results are presented in Table 1, entries 1–4. The impact of different solvents on the reaction's progression was then explored to determine the most suitable solvent after selecting the optimal catalyst quantity. Table 1, entries 6–9, displays the outcomes of this investigation. Subsequently, diverse lighting conditions were examined to achieve optimal illumination for the model reaction, and the results are depicted in entries 8–12. Given the remarkable efficiency of the reaction and to align with the principles of green chemistry, additional derivatives were synthesized under similar conditions to fulfill the specified objectives.

3.3.1. Catalytic activity of the fabricated catalyst in propargylamine synthesis. After thorough investigation and experimental optimization of the oxidation conditions for benzyl alcohol using the Cu–CuO–Cu_2O/GLC heterostructure catalyst, additional benzyl alcohol derivatives were synthesized under optimal conditions, employing various light sources to assess the catalyst's performance (Table 2). The findings affirm that the Cu–CuO–Cu_2O/GLC heterostructure exhibits activation capability in the presence of visible light, blue light, and sunlight. This is attributed to its narrow band gap and the remarkable built-in electric field at the CuO and Cu_2O interface.

3.4. Proposed mechanism

The potential charge transfer across the hetero-interface over the CuO/Cu/Cu_2O anchored GLC S-scheme heterojunction under irradiation is elucidated in Fig. 6, combined with the aforementioned results. Mott–Schottky calculations reveal that the Fermi level of Cu_2O is initially higher than that of CuO before contact (Fig. 6). Upon contact, due to the disparity in Fermi energy levels, electrons tend to migrate spontaneously from CuO to Cu_2O until their Fermi levels reach equilibrium. Additionally, the directional movement of electrons induces the bending of energy bands and generates an IEF between the interfaces of the two semiconductors (Fig. 6).[20,21,25,56,57] In this scenario, Cu nanoparticles act as solid-state electron mediators, facilitating charge transfer in the ternary S-scheme heterojunction.[58–60] Furthermore, GLC serves as an electron sink, capable of trapping photogenerated electrons to expedite charge transfer and separation. Under irradiation, electrons are photo-excited from the VB to the CB of CuO and Cu_2O, respectively. Through the combined effect of IEF and band bending, the photo-generated electrons in the CB of CuO preferentially recombine with the holes in the VB of Cu_2O, thus promoting the transfer of photo-generated electrons from the VB to the CB of both CuO and Cu_2O. This process enhances the efficiency of charge separation and the redox ability of the photocatalysis. During the photocatalytic oxidation of benzyl alcohols (BAs), an ionization equilibrium occurs, producing BA^- and H^+.[61–63] These alkoxide anions are adsorbed on the surface of the Cu_2O due to its positively charged surface. Photogenerated electrons can be captured by dissolved O_2 to form $\cdot O_2^-$, which can further react with H^+ to produce other hydroxide-containing derivatives, while leaving photogenerated holes on the surface of CuO. Subsequently, BA^- reacts with photogenerated holes and releases an electron to form carbon radicals. These carbon radicals, being less stable, tend to react

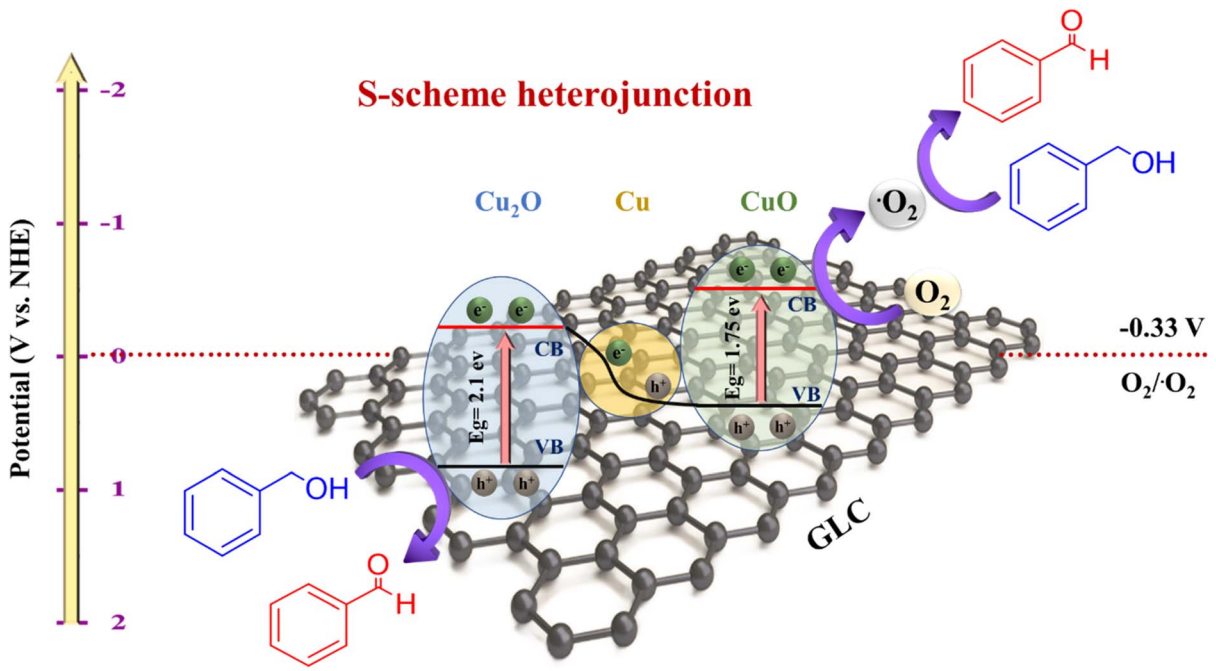

Fig. 6 Proposed photoreaction mechanism for the photocatalytic oxidation of BA into BAD over the CuO/Cu/Cu_2O anchored GLC S-scheme heterojunction under blue LED irradiation.

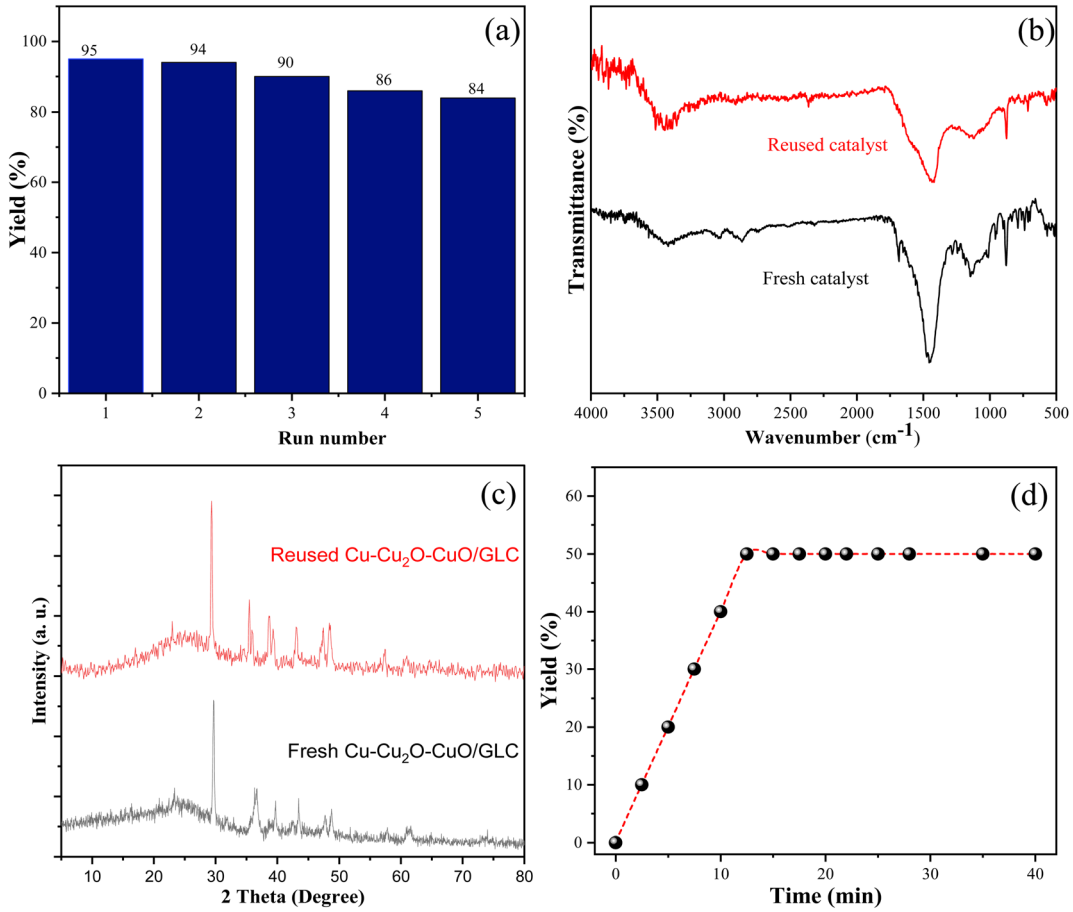

Fig. 7 Recycling experiment of the photocatalyst (a), FT-IR spectra (b), XRD patterns (c) and leaching experiment of the Cu–CuO–Cu_2O/GLC heterostructure photocatalyst (d).

with holes to lose another electron, leading to their reconstruction and facilitating the dehydrogenation step to produce the corresponding aldehyde (see Fig. 6).

3.5. Photocatalytic stability and reusability

The simple recovery and reusability of the catalyst are crucial aspects from the perspectives of economics, industry, and sustainable chemistry. Post-reaction, the catalyst was efficiently separated from the reaction mixture through centrifugation. Subsequently, the isolated catalyst was washed with hot ethanol and air-dried at ambient temperature. Remarkably, the dried catalyst exhibited consistent catalytic performance over 5 successive cycles in the photocatalytic reaction of alcohol oxidation, as depicted in Fig. 7a. Furthermore, the physicochemical stability of the prepared photocatalyst, even after 5 cycles of reuse, was corroborated by FTIR spectra (Fig. 7b) and XRD patterns (Fig. 7c). To assess the heterogeneity of the catalyst, a hot filtration test was conducted in the reaction environment (Fig. 7d). After 5 minutes (half the reaction time), the catalyst was completely separated using filter paper, and the reaction was allowed to continue. Notably, no progress was observed in the reaction without the catalyst for 40 minutes (monitored by TLC), indicating the heterogeneous nature of the catalyst.

3.6. Comparison with other heterogeneous photocatalysts

Table 3 provides a comparison of the photocatalytic activity of the Cu–CuO–Cu_2O/GLC heterostructure with some previously

Table 3 Comparison with related photocatalysts reported in the literature

Entry	Catalyst	Conditions	Time (h:min)	Yield (%)	Ref.
1	Cu nanoclusters/TiO_2/activated carbon nanocomposite	Visible light, acetonitrile	06:00	100	64
3	$TiO_2(P_{25})$-ZnO/Fe^{3+}	$NaNO_3$, blue light, acetonitrile	02:00	100	65
4	Oxy-g-CND@HPU	TBHP, blue light, acetonitrile	03:00	90	66
5	Cu–CuO–Cu_2O/GLC heterostructure	TBHP, visible light, acetonitrile	00:20	95	This work

reported heterogeneous photocatalysts. This novel photocatalyst exhibits notable features including high stability, a straightforward synthesis process, and reusability. Notably, it is constructed from cost-effective and environmentally friendly materials such as basil seeds. While the reported photocatalysts offer certain advantages such as eliminating the need for additional chemical oxidants, shortened assay times, and operating under mild conditions, the Cu–CuO–Cu_2O/GLC heterostructure presents a compelling alternative with its unique set of benefits.

4. Conclusions

In this study, we successfully designed, fabricated, and characterized a heterostructure photocatalyst featuring Cu–CuO–Cu_2O/GLC. This innovative design incorporates a hydrogel template derived from abundantly available basil seeds. The synchronous S-scheme implemented in this design significantly contributes to the improved photocatalytic performance of Cu–CuO–Cu_2O/GLC heterojunctions. These processes are notably enhanced through the collaborative effects of naturally occurring GLC, the synergistic effect of copper-shared atoms within the S-scheme heterointerface, and the built-in electric field. This synergy leads to improved light utilization efficiency and the effective separation of photogenerated electron–hole pairs. Under visible light at room temperature, the catalyst exhibited exceptional catalytic activity in the oxidation of various alcohols to their corresponding aldehydes. Furthermore, the catalyst demonstrated ease of reusability, recyclability, and a straightforward workup approach, underscoring the practical advantages of this technology. With the copper species in the appropriate oxidation state, the developed catalysts show promise for diverse catalytic applications. In summary, our findings suggest that this catalyst stands out as a competitive candidate for a broad spectrum of reactions and applications in the future.

Data availability

Data are available from the corresponding author on request.

Conflicts of interest

There are no conflicts to declare.

References

1 M.-Z. Jia, *et al.*, Switchable ROS species regulation facilitates the selective oxidation of benzyl alcohols enabled by an organic photocatalyst, *ACS Sustain. Chem. Eng.*, 2022, **10**(29), 9591–9599.
2 M.-Y. Qi, *et al.*, Photoredox coupling of benzyl alcohol oxidation with CO2 reduction over CdS/TiO2 heterostructure under visible light irradiation, *Appl. Catal. B Environ.*, 2022, **307**, 121158.
3 A. E. ElMetwally, *et al.*, Plasmon-Enhanced Photocatalytic Oxidation of Benzyl Alcohol to Benzaldehyde Using BiVO4/BiOBr/Au Nanosheets, *ACS Appl. Nano Mater.*, 2023, **6**(7), 5909–5917.
4 F. Wang, *et al.*, The effect of halogen on BiOX (X = Cl, Br, I)/Bi2WO6 heterojunction for visible-light-driven photocatalytic benzyl alcohol selective oxidation, *Appl. Catal., A*, 2018, **567**, 65–72.
5 H. She, *et al.*, Nickel-doped excess oxygen defect titanium dioxide for efficient selective photocatalytic oxidation of benzyl alcohol, *ACS Sustain. Chem. Eng.*, 2018, **6**(9), 11939–11948.
6 C. Meng, *et al.*, Photocatalytic oxidation of benzyl alcohol by homogeneous CuCl2/solvent: a model system to explore the role of molecular oxygen, *ACS Catal.*, 2015, **5**(6), 3760–3766.
7 Q. Shi, *et al.*, Plasmonic Au Nanoparticle of a Au/TiO2–C3N4 Heterojunction Boosts up Photooxidation of Benzyl Alcohol Using LED Light, *ACS Appl. Mater. Interfaces*, 2023, **15**(25), 30161–30169.
8 Q. Shi, *et al.*, In-situ exfoliation and assembly of 2D/2D g-C3N4/TiO2(B) hierarchical microflower: enhanced photooxidation of benzyl alcohol under visible light, *Carbon*, 2022, **196**, 401–409.
9 X. Bao, *et al.*, TiO2/Ti3C2 as an efficient photocatalyst for selective oxidation of benzyl alcohol to benzaldehyde, *Appl. Catal. B Environ.*, 2021, **286**, 119885.
10 J. Wu, *et al.*, Poly(dibenzothiophene-S,S-dioxide)-Fe2O3 heterojunction for photocatalytic hydrogen production coupled with selective oxidation of benzyl alcohol, *Appl. Catal. B Environ.*, 2023, **332**, 122741.
11 J. Wu, *et al.*, Poly (dibenzothiophene-S, S-dioxide)-Fe2O3 heterojunction for photocatalytic hydrogen production coupled with selective oxidation of benzyl alcohol, *Appl. Catal. B Environ.*, 2023, **332**, 122741.
12 G. Zhang, *et al.*, Internal electric field engineering of bifunctional 2D/2D heterojunction photocatalyst for cooperative H2 production and alcohol conversion, *Appl. Catal. B Environ.*, 2023, **331**, 122725.
13 E. S. Paghaleh, *et al.*, Green synthesis of stable CuFe2O4/CuO-rGO heterostructure photocatalyst using basil seeds as chemo-reactors for improved oxytetracycline degradation, *J. Environ. Chem. Eng.*, 2023, **11**(5), 110676.
14 K. Dashtian, *et al.*, A review on metal-organic frameworks photoelectrochemistry: a headlight for future applications, *Coord. Chem. Rev.*, 2021, **445**, 214097.
15 M. Huang, *et al.*, Rational fabrication of cadmium-sulfide/graphitic-carbon-nitride/hematite photocatalyst with type II and Z-scheme tandem heterojunctions to promote photocatalytic carbon dioxide reduction, *J. Colloid Interface Sci.*, 2022, **628**, 129–140.
16 H. Li, *et al.*, Preparation of solid-state Z-scheme Bi2MoO6/MO (MCu, Co3/4, or Ni) heterojunctions with internal electric field-improved performance in photocatalysis, *Appl. Catal. B Environ.*, 2016, **188**, 313–323.
17 J. Chen, *et al.*, Internal electric field promoted NCDs/BiOBr/AgBr Z-scheme heterojunction with rich oxygen vacancies for efficient photocatalytic degradation of tetracycline and reduction of Cr (VI), *J. Environ. Chem. Eng.*, 2024, 112476.

18 N. Zhang, *et al.*, Toward improving the graphene–semiconductor composite photoactivity via the addition of metal ions as generic interfacial mediator, *ACS Nano*, 2014, **8**(1), 623–633.
19 E.-Z. Deng, *et al.*, Engineering a Z-Scheme Heterostructure on ZnIn2S4@ NH2-MIL-125 Composites for Boosting the Photocatalytic Performance, *Inorg. Chem.*, 2024, **63**(2), 1449–1461.
20 L. Li, *et al.*, Ascorbic-acid-assisted in-situ construction of S-scheme CuO/Cu2O hetero-nanosheets with active Cu (II)-O-Cu (I) bridges for efficient CO2 photoreduction, *Appl. Surf. Sci.*, 2024, **651**, 159220.
21 B. Dai, *et al.*, Photocatalytic reduction of CO2 and degradation of Bisphenol-S by g-C3N4/Cu2O@ Cu S-scheme heterojunction: study on the photocatalytic performance and mechanism insight, *Carbon*, 2022, **193**, 272–284.
22 P. Sarkar, S. De and S. Neogi, Microwave assisted facile fabrication of dual Z-scheme g-C3N4/ZnFe2O4/Bi2S3 photocatalyst for peroxymonosulphate mediated degradation of 2,4,6-trichlorophenol: the mechanistic insights, *Appl. Catal. B Environ.*, 2022, **307**, 121165.
23 H. Yang, *et al.*, Mechanism insight into triple S-Scheme intermolecular carbon nitride homojunction with robust built-in electric field for highly enhanced photocatalytic hydrogen evolution, *Chem. Eng. J.*, 2024, **481**, 148297.
24 X. Yang, *et al.*, A 2D–2D BiO2−x/Bi2WO6 composite assembled via layer on layer and application in the abatement of the aqueous tetracycline, *J. Alloys Compd.*, 2023, **935**, 168061.
25 A. Shamloufard, *et al.*, S-scheme NIR-edge Ag3CuS2/VO2 heterostructure for photo-oxidation/reduction of methylene blue/Cr (VI), *Appl. Surf. Sci.*, 2022, **590**, 153118.
26 H. Wen, *et al.*, Directing charge transfer in a chemical-bonded Ni/Cd0.7Mn0.3S Schottky heterojunction for selective photocatalytic oxidation of benzyl alcohol structural organic platform molecules coupled with hydrogen evolution reaction, *Applied Catalysis B: Environment and Energy*, 2024, **345**, 123641.
27 D. Gholami, *et al.*, In situ growth of CuFeS2/CuS bridged heterojunction catalyst with mixed redox-couple cations for excellent photocatalytic degradation of organophosphate insecticide: CFD and DFT modeling, *Chem. Eng. J.*, 2023, **461**, 141950.
28 Q. Su, *et al.*, Heterojunction photocatalysts based on 2D materials: the role of configuration, *Adv. Sustain. Syst.*, 2020, **4**(9), 2000130.
29 S. Das, *et al.*, Magnetically separable MnFeCoNiCu-based high entropy alloy nanoparticles for photocatalytic oxidation of antibiotic cocktails in different aqueous matrices, *Chem. Eng. J.*, 2023, **476**, 146719.
30 D. Gogoi, *et al.*, Cu and CoFe2O4 nanoparticles decorated hierarchical porous carbon: an excellent catalyst for reduction of nitroaromatics and microwave-assisted antibiotic degradation, *Appl. Catal. B Environ.*, 2022, **312**, 121407.
31 M.-H. Sun, *et al.*, Applications of hierarchically structured porous materials from energy storage and conversion, catalysis, photocatalysis, adsorption, separation, and sensing to biomedicine, *Chem. Soc. Rev.*, 2016, **45**(12), 3479–3563.
32 H. Xu, *et al.*, Supports promote single-atom catalysts toward advanced electrocatalysis, *Coord. Chem. Rev.*, 2022, **451**, 214261.
33 Q. Xiang, J. Yu and M. Jaroniec, Graphene-based semiconductor photocatalysts, *Chem. Soc. Rev.*, 2012, **41**(2), 782–796.
34 F. Maldonado-Hódar, *et al.*, Catalytic graphitization of carbon aerogels by transition metals, *Langmuir*, 2000, **16**(9), 4367–4373.
35 X. Li, *et al.*, Fabrication of ultrathin lily-like NiCo2O4 nanosheets via mooring NiCo bimetallic oxide on waste biomass-derived carbon for highly efficient removal of phenolic pollutants, *Chem. Eng. J.*, 2022, **441**, 136066.
36 B. Liu, *et al.*, Graphene-like porous carbon nanosheets for ultra-high rate performance supercapacitors and efficient oxygen reduction electrocatalysts, *J. Power Sources*, 2020, **456**, 227999.
37 Y. Lin, *et al.*, Nitrogen and Sulfur Co-Doped Graphene-Like Carbon from Industrial Dye Wastewater for Use as a High-Performance Supercapacitor Electrode, *Global Chall.*, 2019, **3**(11), 1900043.
38 A. Aryasomayajula, *et al.*, Robust chemiresistive sensor for continuous monitoring of free chlorine using graphene-like carbon, *ACS Sens.*, 2018, **3**(2), 451–457.
39 M. Yang, *et al.*, Graphene and graphene-like carbon nanomaterials-based electrochemical biosensors for phytohormone detection, *Carbon Lett.*, 2023, **33**(5), 1343–1358.
40 Q. Liu and X. Li, Molten salt synthesis of porous graphene-like carbons as peroxydisulfate catalyst for the efficient removal of rhodamine B dye, *Environ. Sci. Pollut. Res.*, 2024, 1–13.
41 N. Sharma, *et al.*, Nanotubular hard carbon derived from renewable natural seed gel for high performance sodium-ion battery anode, *ChemistrySelect*, 2017, **2**(23), 6909–6915.
42 S. M. Ghoreishian, *et al.*, Full-spectrum-responsive Bi2S3@CdS S-scheme heterostructure with intimated ultrathin RGO toward photocatalytic Cr (VI) reduction and H2O2 production: experimental and DFT studies, *Chem. Eng. J.*, 2021, **419**, 129530.
43 J.-R. Zheng, *et al.*, S-scheme heterojunction CeO2/TiO2 modified by reduced graphene oxide (rGO) as charge transfer route for integrated photothermal catalytic oxidation of Hg0, *Fuel*, 2023, **343**, 127973.
44 S. Rana, *et al.*, Ionic liquid assisted growth of poly (3, 4-ethylenedioxythiophene)/reduced graphene oxide based electrode: an improved electro-catalytic performance for the detection of organophosphorus pesticides in beverages, *Arab. J. Chem.*, 2019, **12**(7), 1121–1133.
45 N. Sedefoglu, *et al.*, Green synthesized CuO nanoparticles using macrofungi extracts: characterization, nanofertilizer

and antibacterial effects, *Mater. Chem. Phys.*, 2023, **309**, 128393.

46 Y. Cheng, *et al.*, Hyaluronic acid-coated Bi: Cu2O: an H2S-responsive agent for colon cancer with targeted delivery and enhanced photothermal performance, *J. Nanobiotechnol.*, 2022, **20**(1), 1–14.

47 H. Park, *et al.*, Lithiophilic surface treatment of metal-and metallic compound-based frameworks by gas nitriding for lithium metal batteries, *J. Power Sources*, 2020, **477**, 228776.

48 H. H. Gahruie, *et al.*, Study on hydrophobic modification of basil seed gum-based (BSG) films by octenyl succinate anhydride (OSA), *Carbohydr. Polym.*, 2019, **219**, 155–161.

49 F. V. Cabral, *et al.*, Pluronic F-127 hydrogels containing copper oxide nanoparticles and a nitric oxide donor to treat skin cancer, *Pharmaceutics*, 2023, **15**(7), 1971.

50 J. Kang, *et al.*, New studies on gum ghatti (Anogeissus latifolia) part I. Fractionation, chemical and physical characterization of the gum, *Food Hydrocolloids*, 2011, **25**(8), 1984–1990.

51 H. H. Gahruie, *et al.*, Study on hydrophobic modification of basil seed gum-based (BSG) films by octenyl succinate anhydride (OSA), *Carbohydr. Polym.*, 2019, **219**, 155–161.

52 A. Dandia, *et al.*, Microwave-assisted nanocatalysis: a CuO NPs/rGO composite as an efficient and recyclable catalyst for the Petasis-borono–Mannich reaction, *RSC Adv.*, 2018, **8**(53), 30280–30288.

53 A. Nowak, *et al.*, Physicochemical and antibacterial characterization of ionocity Ag/Cu powder nanoparticles, *Mater. Charact.*, 2016, **117**, 9–16.

54 Y. Zhang, *et al.*, A novel nonenzymatic glucose sensor based on magnetic copper ferrite immobilized on multiwalled carbon nanotubes, *Anal. Methods*, 2015, **7**(6), 2360–2366.

55 Y. Zhao, *et al.*, High Catalytic Activity in the Phenol Hydroxylation of Magnetically Separable CuFe2O4–Reduced Graphene Oxide, *Ind. Eng. Chem. Res.*, 2014, **53**, 12566–12574.

56 S. Parsaei, *et al.*, Bi-metal-organic framework-derived S-scheme InP/CuO-C heterostructure for robust photocatalytic degradation of ciprofloxacin in a microfluidic photoreactor, *Chem. Eng. J.*, 2023, **475**, 146448.

57 S. Zamani, *et al.*, WO3/Ag/ZnO S-scheme heterostructure thin film spinning disc photoreactor for intensified photodegradation of cephalexin antibiotic, *Chemosphere*, 2022, **307**, 135812.

58 J. Yang, *et al.*, Efficient hydrogen generation of vector Z-scheme CaTiO3/Cu/TiO2 photocatalyst assisted by cocatalyst Cu nanoparticles, *J. Colloid Interface Sci.*, 2022, **605**, 373–384.

59 Z. Xu, *et al.*, Carbon dots as solid-state electron mediator and electron acceptor in S-scheme heterojunction for boosted photocatalytic hydrogen evolution, *Appl. Surf. Sci.*, 2022, **595**, 153482.

60 H. Zhang, *et al.*, Metal Sulfide S-Scheme Homojunction for Photocatalytic Selective Phenylcarbinol Oxidation, *Adv. Sci.*, 2024, **11**(17), 2400099.

61 C. Zheng, *et al.*, Selective photocatalytic oxidation of benzyl alcohol into benzaldehyde with high selectivity and conversion ratio over Bi4O5Br2 nanoflakes under blue LED irradiation, *Appl. Catal. B Environ.*, 2017, **205**, 201–210.

62 J. Tian, *et al.*, Photocatalytic hydrogen production coupled with selective benzyl alcohol oxidation via WOx/CdS S-scheme heterojunction, *Int. J. Hydrogen Energy*, 2024, **74**, 31–38.

63 Z. Zhang, *et al.*, Photocatalytic activity of CuBi2O4/WO3 pn heterojunction photocatalysts in benzyl alcohol oxidation to benzaldehyde, *J. Alloys Compd.*, 2023, **968**, 172209.

64 M. Farrag and R. Yahya, Selective solar photocatalytic oxidation of benzyl alcohol to benzaldehyde over monodispersed Cu nanoclusters/TiO2/activated carbon nanocomposite, *J. Photochem. Photobiol., A*, 2020, **396**, 112527.

65 S. Fallahnezhad and A. Amoozadeh, Magnetic field-assisted photochemical oxidation of benzyl alcohol to corresponding aldehydes by introducing TiO2 (P25)-ZnO/Fe3+ as a novel nanophotocatalyst, *J. Chin. Chem. Soc.*, 2021, **68**(11), 2085–2092.

66 R. Bayan and N. Karak, Bio-based hyperbranched polymer-supported oxygeneous graphitic-carbon nitride dot as heterogeneous metal-free solar light photocatalyst for oxidation and reduction reactions, *Appl. Surf. Sci.*, 2020, **514**, 145909.